Residual ion tracking in ThomX

Danylo Radevych, Alexis Gamelin, Christelle Bruni

Abstract

This work was aimed to update software for ion tracking in the ThomX ring by adding a tracking in the electric field of electrodes, dipole and quadrupole magnetic field to the existing tracking with only beam-ion interaction. Corrections for the curved parts of the ring where implementation of the curvilinear frame is required were also made. The developed routine allowed to estimate the number of singly-ionized ions at each turn of tracking, as well as compare the cases with and without the electrodes, and small gaps between the main cycles of the bunch circulation in the ring when the bunch is absent.

1 Introduction

1.1 ThomX

The dynamic evolution and increasing performance of laser and particle systems have opened the way to compact radiation sources based on Compton backscattering (CBS) [1]. The CBS scheme has several attractive characteristics: it provides the most efficient photon energy boost, so that hard X-rays can be produced with a comparatively low energy electron beam resulting in very compact and low cost devices. This is extremely important in a view of the integration of such a radiation source in a "non-laboratory" environment, like a hospital or a museum.

The ThomX project is taking advantage of the preeminent technology in accelerator and laser fields developed in France. The objective is to design and build a demonstrator with cutting edge performances compared to similar projects either currently in operation or planned. This project is a direct outcome of the sustained efforts made by several laboratories to achieve a high amplification of laser pulses by stacking them in a passive optical resonator.

The basic ThomX layout is shown in Fig. 1. The circumference of the ThomX ring is 17986.68 mm ($\approx$ 18 m). During the one cycle, only one electron bunch is circulating in the ring.

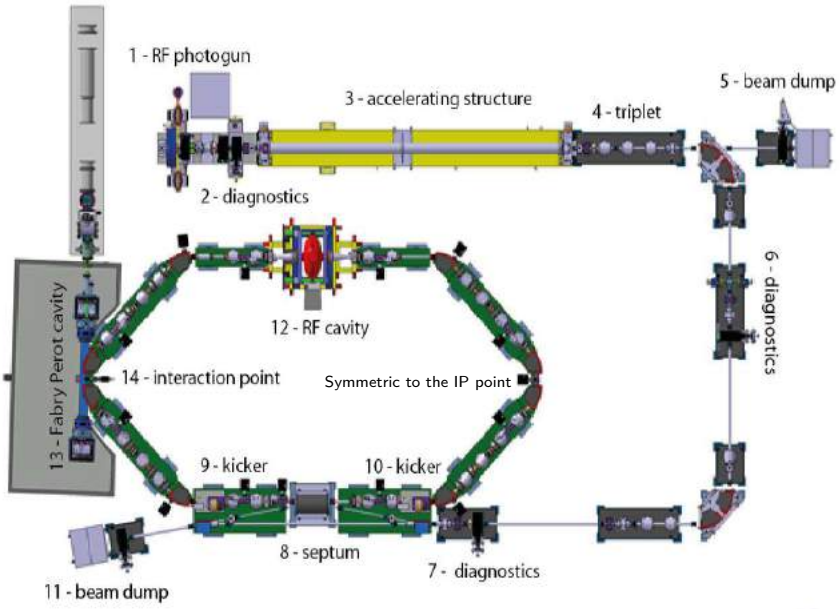

Figure 1: ThomX layout.

1.2 Ion tracking

Since the vacuum in the pipeline is not ideal and pressure inside is $p_0 \approx 3.06 \cdot 10^{-8}$ Pa, ionization of the residual gas occurs during the every passage of the electron bunch. Ions that are created very close to the beam centerline (roughly within the range of one σ of the bunch transverse distribution) can be trapped in the beam space charge potential [2]. In Fig. 2 (a), we see that such ions with positive value of x-coordinate have negative variation of velocity Δv_x, and, vice versa, ions with negative value of x-coordinate have positive variation Δv_x. They will oscillate around the beam centerline.

The presence of the ions near the beam centerline may generate all sorts of ill effects: reduced beam lifetime (increased pressure); emittance growth; losses through excitation of resonances; coherent beam instabilities [3].

Transverse kicks from the beam-ion interaction can be summarized by the Bassetti-Erskine formula (1), where N_e is the number of electrons in the bunch, x and y are the transverse coordinates of the ion, α, β, and γ are Twiss parameters, ε is the emittance, η, η' are the off-energy functions, and $\tilde{\sigma_\varepsilon} = \sigma_E / E_0$ is the relative energy spread, and $w(z)$ is the complex error function [2].

$$\Delta v_y + i\Delta v_x = \sqrt{\frac{\pi}{2\left({\sigma_x}^2 - {\sigma_y}^2\right)}} N_e K \times \\ \times \left[w\left(\frac{x + iy}{\sqrt{2\left({\sigma_x}^2 - {\sigma_y}^2\right)}} \right) - e^{\left(-\left(\frac{x^2}{2{\sigma_x}^2} + \frac{y^2}{2{\sigma_y}^2} \right) \right)} w\left(\frac{x\frac{\sigma_y}{\sigma_x} + iy\frac{\sigma_x}{\sigma_y}}{\sqrt{2\left({\sigma_x}^2 - {\sigma_y}^2\right)}} \right) \right], \quad (1)$$

where

$$\sigma_x = \sqrt{\varepsilon_x \beta_x + \eta^2 {\tilde{\sigma_\varepsilon}}^2},$$
$$\sigma_y = \sqrt{\varepsilon_y \beta_y}.$$

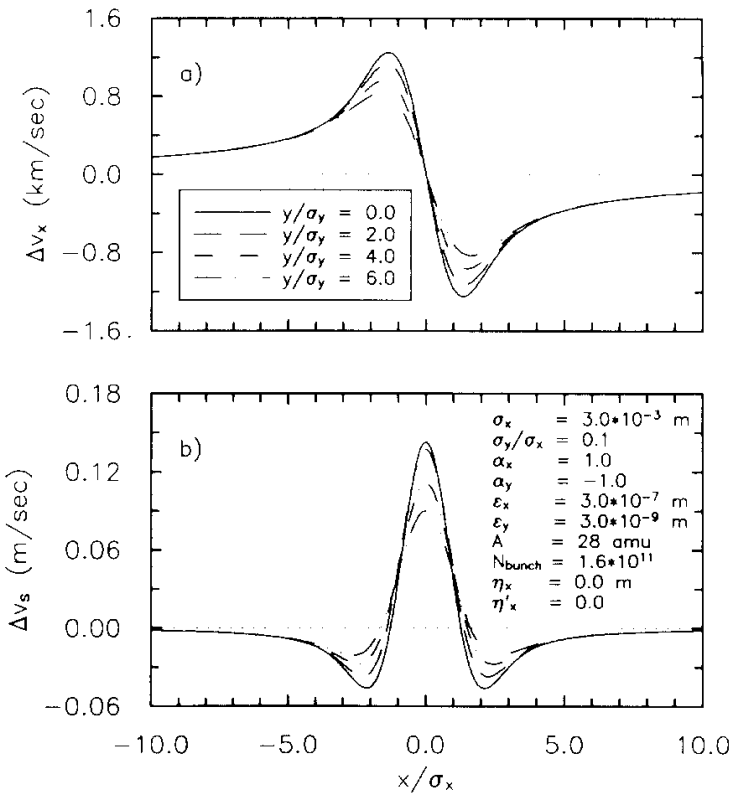

Figure 2: The variation of (a) horizontal kick Δv_x, and (b) the longitudinal kick Δv_s as a function of x for several values of y. In this case the longitudinal kick is such that at $x = 0$ the ion will feel a kick towards a point of minimum β_x [2].

D. Sagan [2] also introduced the longitudinal kick Δv_s that can be evaluated in terms of the transverse kicks (see Eq. (2) and Fig. 2 (b)).

$$\Delta v_s = \left[-\alpha_x \varepsilon_x + \left(\eta \tilde{\sigma}_\varepsilon\right)\left(\eta' \tilde{\sigma}_\varepsilon\right)\right] \frac{\partial \Delta v_x}{\partial x} - \alpha_y \varepsilon_y \frac{\partial \Delta v_y}{\partial y}. \tag{2}$$

Ions' rapid transverse oscillations tend to cancel the effect of the transverse kicks. Even though the effect of the kicks Δv_s is 3 orders below Δv_x or Δv_y, it can accumulate over a relatively long time scales.

Formulas (1) and (2) were deeply analized by Alexis Gamelin and Christelle Bruni in [4]. This work was the starting point for the residual ion tracking. Color maps for the kicks from beam-ion interaction in the ThomX ring are depicted in the Fig. 3. Since the two halves of the ring are symmetric in terms of the beam-ion interaction, we provide the color maps only for the first part assuming that the second half is the same.

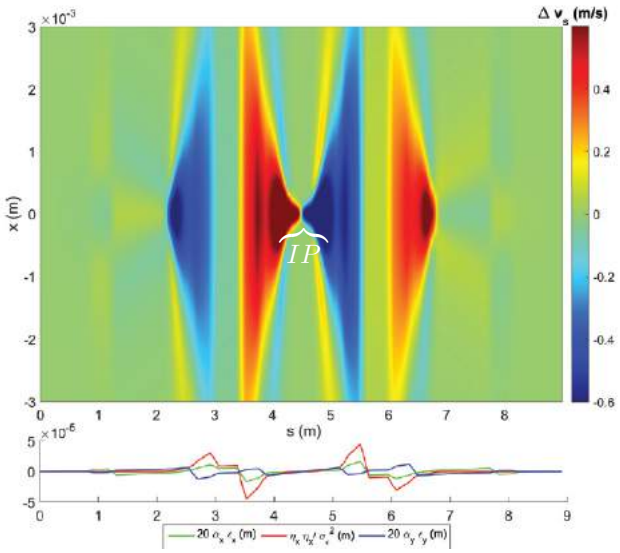

(a) Top: Color map of the longitudinal kick Δv_s vs. horizontal position x and longitudinal position s along the half of the ThomX ring for CO^+ ions (mass number A = 28). Bottom: $\alpha_x \varepsilon_x$ $(y = 0)$ in green, $\left(\eta \tilde{\sigma_\varepsilon}\right)\left(\eta' \tilde{\sigma_\varepsilon}\right)$ in red, and $\alpha_y \varepsilon_y$ $(x = 0)$ in blue vs. longitudinal postion s along the half of the ThomX ring.

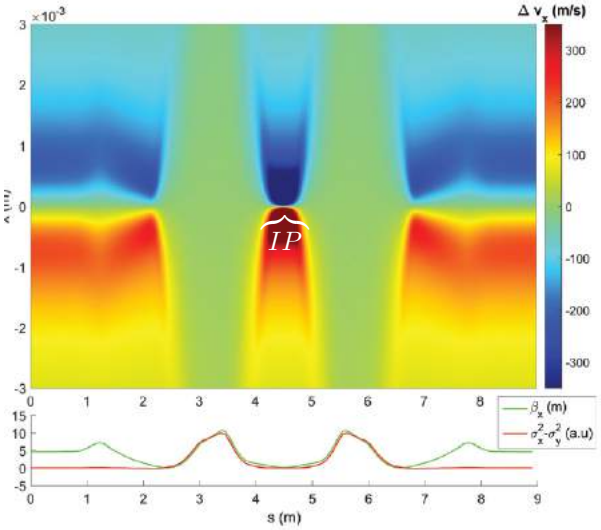

(b) Top: Color map of the horizontal kick Δv_x vs. horizontal position x and longitudinal position s along the half of the ThomX ring. For CO^+ ions (mass number A = 28). Bottom: Twiss parameter β_x in green and ${\sigma_x}^2 - {\sigma_y}^2$ in red (arbitrary units) vs. longitudinal postion s along the half of the ThomX ring.

Figure 3: Kickmap for CO^+ ions with only beam-ion interaction [4].

The central point in the Fig. 3a corresponds to the interaction point (IP) or symmetric to the IP point (IPsym) in the ThomX ring. These colormaps show that ions feel kicks from beam-ion interaction towards the IP or IPsym points in both longitudinal and transverse dimensions.

However, this picture did not represent a real configuration of the ThomX ring since it did not take into consideration the key elements that can clear the ions (electrodes) and trap them (dipole and, in a less degree, quadrupole magnets). Investigation of an influence of the mentioned elements on ion distribution was the aim of this work.

2 Curvilinear coordinates

The formulas (1) and (2) are derived for the such (x, y, s) coordinate system that the s-axis is aligned with the beam centerline, the x-axis is the horizontal axis and the y-axis is the vertical. Further, we will call it as curvilinear frame.

However, when it comes to the kicks in the dipole magnets, where the beam centerline is curved, a direction of the Lorentz force does not represent a direction of the kick in the curvilinear frame. That is why we had to understand how to take into account the rotation of the direction vectors of the frame.

The following paragraphs elaborate the derivation of the equation of motion in a magnetic field in the curvilinear frame.

2.1 Radius vector, velocity, and acceleration in the curvilinear frame

We consider the following curvilinear frame as it is depicted in the Fig. 4 [5].

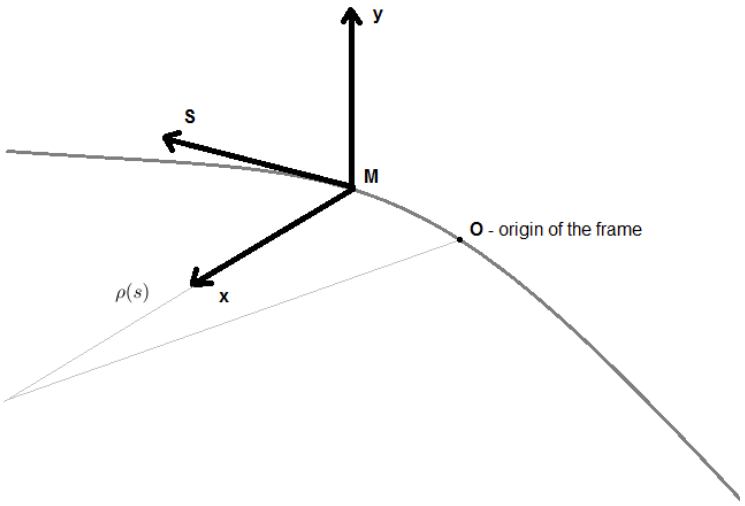

Figure 4: Curvilinear frame.

$$h = \frac{1}{\rho(s)} \text{ – the parameter of a curve; } \rho(s) \text{ is the radius of a curve.} \tag{3}$$

The reference trajectory of the electron bunch represents the s-axis. The origin of the frame at the point O is fixed at the laboratory frame. The s-coordinate of a particle is equal to the path along the reference trajectory of the electron bunch from the point O to the point M.

$\vec{x}$, $\vec{y}$, $\vec{s}$ are unit vectors along the corresponding axes.

Taking into account the rotation of the unit vectors depending on the s-position of a particle, we get the system of equations (4). In this case, we assume that the reference trajectory lies on the same plane and its y-coordinate is always constant and equal to 0.

$$\begin{cases} \dfrac{d\vec{x}}{ds} = -\dfrac{\vec{s}}{\rho} = -h\vec{s}, \\ \dfrac{d\vec{s}}{ds} = \dfrac{\vec{x}}{\rho} = h\vec{x}, \\ \dfrac{d\vec{y}}{ds} = 0. \end{cases} \tag{4}$$

Time derivatives (5) can be expressed with a change of the s-coordinate with time.

$$\begin{cases} \dfrac{d\vec{x}}{dt} = \dfrac{d\vec{x}}{ds}\dot{s} = -h\dot{s}\vec{s}, \\ \dfrac{d\vec{s}}{dt} = \dfrac{d\vec{s}}{ds}\dot{s} = h\dot{s}\vec{x}, \\ \dfrac{d\vec{y}}{dt} = 0. \end{cases} \tag{5}$$

The unit vector $\vec{s}$ is tangent to the trajectory (6).

$$\frac{d\overrightarrow{OM}}{ds} = \vec{s}. \tag{6}$$

The radius vector of a particle is expressed as a sum of the vector from the origin O to the reference point M ($\vec{OM}$) and the vector from the point M to the particle in the xMy-plane (7). The x, y, and s are corresponding coordinates of the particle in the curvilinear frame.

$$\vec{r} = \overrightarrow{OM} + x \cdot \vec{x} + y \cdot \vec{y}. \tag{7}$$

Then velocity of the particle is equal to the derivative of the radius vector $\vec{r}$ with respect to time. The expression (8) is obtained from (5) – (7).

$$\begin{aligned}
\dot{\vec{r}} &= \frac{d\overrightarrow{OM}}{ds} \cdot \frac{ds}{dt} + \dot{x} \cdot \vec{x} + x \cdot \dot{\vec{x}} + +\dot{y} \cdot \vec{y} = \\
&= \dot{s} \cdot \vec{s} + \dot{x} \cdot \vec{x} + x \cdot \dot{\vec{x}} + \dot{y} \cdot \vec{y} = \\
&= \dot{s} \cdot \vec{s} + \dot{x} \cdot \vec{x} - h\dot{s}x \cdot \vec{s} + \dot{y} \cdot \vec{y} = \\
&= \underbrace{\dot{x}}_{v_x} \cdot \vec{x} + \underbrace{\dot{y}}_{v_y} \cdot \vec{y} + \underbrace{\dot{s}(1 - hx)}_{v_s} \cdot \vec{s} = \\
&= \vec{v}.
\end{aligned} \tag{8}$$

An important conclusion is that the s-component of velocity v_s is not equal to the derivative of s with respect to time (9).

$$v_s \neq \dot{s}, \;\; \dot{s} = \frac{v_s}{1 - hx}. \tag{9}$$

The acceleration vector of the particle is equal to the derivative of the velocity vector with respect to time (10).

$$\begin{aligned}
\ddot{\vec{r}} &= \dot{v}_x\vec{x} + v_x\dot{\vec{x}} + \dot{v}_y\vec{y} + \dot{v}_s\vec{s} + v_s\dot{\vec{s}} = \\
&= \dot{v}_x\vec{x} + v_x\vec{x}(-h\dot{s})\vec{s} + \dot{v}_y\vec{y} + \dot{v}_s\vec{s} + v_s(h\dot{s})\vec{x} = \\
&= \begin{bmatrix} \vec{x} & \vec{y} & \vec{s} \end{bmatrix} \begin{bmatrix} \dot{v}_x + v_s(h\dot{s}) \\ \dot{v}_y \\ \dot{v}_s - v_x(h\dot{s}) \end{bmatrix}.
\end{aligned} \tag{10}$$

2.2 Lorentz force in the curvilinear frame

In this section, we intend to write an expression for the acceleration of a particle by Lorentz force in the curvilinear frame.

Let us consider a general magnetic field with the components B_i, an electric charge of the particle q, and its mass m.

Since unit vectors $\vec{x}$, $\vec{y}$, and $\vec{s}$ are perpendicular to each other, an expression for the vector product in the considered curvilinear frame is the same as in the ordinary Cartesian frame (11).

$$\begin{aligned}
\ddot{\vec{r}} &= \frac{q}{m} \begin{vmatrix} \vec{x} & \vec{y} & \vec{s} \\ v_x & v_y & v_s \\ B_x & B_y & B_s \end{vmatrix} = \\
&= \frac{q}{m} \begin{bmatrix} v_yB_s - v_sB_y \\ v_sB_x - v_xB_s \\ v_xB_y - B_xv_y \end{bmatrix}.
\end{aligned} \tag{11}$$

Taking the expressions for the acceleration vector components from (10) on the left hand side in (11), we get the system (12).

$$\begin{cases} \dot{v}_x + \underbrace{v_s h \dot{s}}_{correction} = v_y \dfrac{q}{m} B_s - v_s \dfrac{q}{m} B_y, \\ \dot{v}_y = v_s \dfrac{q}{m} B_x - v_x \dfrac{q}{m} B_s, \\ \dot{v}_s - \underbrace{v_x h \dot{s}}_{correction} = v_x \dfrac{q}{m} B_y - v_y \dfrac{q}{m} B_x. \end{cases} \tag{12}$$

Underlined additional components distinguish the curvilinear frame from Cartesian coordinates. The next system of equations (13) is obtained by moving the mentioned components to the right.

$$\begin{cases} \dot{v}_x = v_y \dfrac{q}{m} B_s - v_s \dfrac{q}{m} B_y - v_s \underline{\dot{s}} \dfrac{1}{\rho}, \\ \dot{v}_y = v_s \dfrac{q}{m} B_x - v_x \dfrac{q}{m} B_s, \\ \dot{v}_s = v_x \dfrac{q}{m} B_y - v_y \dfrac{q}{m} B_x + v_x \underline{\dot{s}} \dfrac{1}{\rho}. \end{cases} \tag{13}$$

The expression (14) is used to remove the derivative $\dot{s}$ from (13) and get the final system of equations (15).

$$\dot{s} = \frac{v_s}{1 - hx}. \tag{14}$$

$$\begin{cases} \dot{v}_x = v_y \dfrac{q}{m} B_s - v_s \dfrac{q}{m} B_y - \dfrac{{v_s}^2}{\rho - x}, \\ \dot{v}_y = v_s \dfrac{q}{m} B_x - v_x \dfrac{q}{m} B_s, \\ \dot{v}_s = v_x \dfrac{q}{m} B_y - v_y \dfrac{q}{m} B_x + \dfrac{v_x v_s}{\rho - x}. \end{cases} \tag{15}$$

2.3 Dipole magnetic field in the curvilinear frame

In the particular case of a dipole magnet in a ring accelerator, the dipole magnetic field is directed along the y-axis (16).

$$\vec{B} = \{0,\ B_y,\ 0\}. \tag{16}$$

Then the x- and s-components of the B-field from the system (15) are absent in the system (17).

$$\begin{cases} \dot{v}_x = -v_s \dfrac{q}{m} B_y - \dfrac{{v_s}^2}{\rho - x}, \\ \dot{v}_y = 0, \\ \dot{v}_s = v_x \dfrac{q}{m} B_y + \dfrac{v_x v_s}{\rho - x}. \end{cases} \tag{17}$$

The radius of curvature ρ must be expressed from the equation for magnetic rigidity (18) [6] with electron bunch reference momentum p_e and electron electric charge e.

$$\begin{aligned} B_y \rho &= \frac{p_e}{e}, \\ \rho &= \frac{p_e}{e B_y}. \end{aligned} \tag{18}$$

It allows us to rewrite the system of equations (17) for the system (19), where all the physical values can be computed.

$$\begin{cases} \dot{v}_x &= -v_s \dfrac{q}{m} B_y - \dfrac{{v_s}^2}{\frac{p_e}{eB_y} - x}, \\ \dot{v}_y &= 0, \\ \dot{v}_s &= v_x \dfrac{q}{m} B_y + \dfrac{v_x v_s}{\frac{p_e}{eB_y} - x}. \end{cases} \tag{19}$$

Finally, we present the full system of equations (20).

$$\begin{cases} \dot{x} &= v_x, \\ \dot{y} &= v_y, \\ \dot{s} &= \dfrac{v_s}{1 - \frac{eB_y}{p_e} x}, \\ \dot{v}_x &= -v_s \dfrac{q}{m} B_y - \dfrac{{v_s}^2}{\frac{p_e}{eB_y} - x}, \\ \dot{v}_y &= 0, \\ \dot{v}_s &= v_x \dfrac{q}{m} B_y + \dfrac{v_x v_s}{\frac{p_e}{eB_y} - x}. \end{cases} \tag{20}$$

2.4 Dimensionless system of equations for the x- and s-axes in a dipole magnetic field in the curvilinear frame

For the numerical purposes, sometimes it is required to make the system of differential equations (21) dimensionless. In this paragraph, we omit the y-components since the equations for them in the dipole magnetic field are the same as in Cartesian coordinates.

$$\begin{cases} \dot{x} &= v_x, \\ \dot{s} &= \dfrac{v_s}{1 - \frac{1}{\rho} x}, \\ \dot{v}_x &= -v_s \dfrac{q}{m} B_y - \dfrac{{v_s}^2}{\rho - x}, \\ \dot{v}_s &= v_x \dfrac{q}{m} B_y + \dfrac{v_x v_s}{\rho - x}. \end{cases} \tag{21}$$

The time variable t can be replaced by a dimensionless parameter λ multiplied by some reference time τ (e.g., time of the one turn of an electron bunch in the ring) (22).

$$t = \tau \cdot \lambda. \tag{22}$$

Considering electrons relativistic and assuming that their velocity is equal to the speed of light ($v_e \approx c$), we can replace the coordinates $x(t)$, $s(t)$ and velocities $v_x(t)$, $v_s(t)$ by dimensionless functions of the parameter λ: $\xi(\lambda)$, $\eta(\lambda)$, $\varkappa_\xi(\lambda)$, and $\varkappa_\eta(\lambda)$ respectively (23). In this case, the speed of light c is arbitrary chosen characteristic velocity.

$$\begin{cases} x &= c\tau \cdot \xi(\lambda), \\ s &= c\tau \cdot \eta(\lambda), \\ v_x &= c \cdot \varkappa_\xi(\lambda), \\ v_s &= c \cdot \varkappa_\eta(\lambda). \end{cases} \tag{23}$$

Then time derivatives must be expressed through the derivatives with respect to the parameter λ (24).

$$\begin{cases} \dot{x} &= c \cdot \xi'(\lambda), \\ \dot{s} &= c \cdot \eta'(\lambda), \\ \dot{v}_x &= \dfrac{c}{\tau} \cdot \varkappa_\xi{}'(\lambda), \\ \dot{v}_s &= \dfrac{c}{\tau} \cdot \varkappa_\eta{}'(\lambda). \end{cases} \tag{24}$$

The final dimensionless system of equations (25) is obtained from (21) – (24).

$$\begin{cases} \xi'(\lambda) &= \varkappa_\xi(\lambda), \\ \eta'(\lambda) &= \dfrac{\varkappa_\eta(\lambda)}{1 - \frac{c\tau \cdot \xi(\lambda)}{\rho}}, \\ \varkappa_\xi{}'(\lambda) &= \tau \cdot \left[-\varkappa_\eta(\lambda)\dfrac{q}{m}B_y - \dfrac{c \cdot \varkappa_\eta{}^2(\lambda)}{\rho - c\tau \cdot \xi(\lambda)} \right], \\ \varkappa_\eta{}'(\lambda) &= \tau \cdot \left[\varkappa_\xi(\lambda)\dfrac{q}{m}B_y + \dfrac{c \cdot \varkappa_\xi(\lambda)\varkappa_\eta(\lambda)}{\rho - c\tau \cdot \xi(\lambda)} \right]. \end{cases} \tag{25}$$

2.5 Quadrupole magnetic field in the curvilinear frame

Quadrupole magnets of the ThomX ring are placed on the straight sections, where $\rho \to \infty$. Thus the derivation of the equation of motion is not complicated.

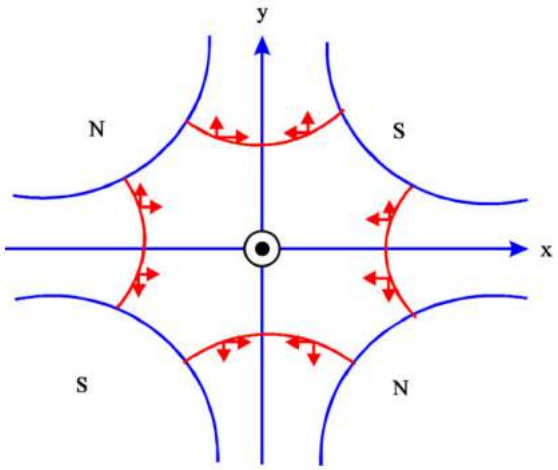

Figure 5: Axis directions inside a quadrupole magnet [6].

For the axes chosen as it is depicted in the Fig. 5, equations for the $x-$ and $y-$components of the quadrupole magnetic field will be the following (26) [6].

$$\begin{aligned} B_x &= -gy, \\ B_y &= -gx. \end{aligned} \tag{26}$$

g is a gradient of the quadrupole magnet. It can be estimated from the equation (27) if the focusing strength of the magnet k is known.

$$k = \frac{g}{p_e/e}. \tag{27}$$

p_e and e are the momentum and charge of the reference particle that moves along the s-axis of the curvilinear frame.

Since quadrupoles are placed on the straight parts of the ring, the equations (15) are simplified. The full system of differential equations is the same as in the Cartesian frame (28).

$$\begin{cases} \dot{x} &= v_x, \\ \dot{y} &= v_y, \\ \dot{s} &= v_s, \\ \dot{v}_x &= \frac{q}{m}\Big(v_y B_s - v_s B_y\Big), \\ \dot{v}_y &= \frac{q}{m}\Big(v_s B_x - v_x B_s\Big), \\ \dot{v}_s &= \frac{q}{m}\Big(v_x B_y - v_y B_x\Big). \end{cases} \tag{28}$$

Taking into account $B_s = 0$ and equations (26), we get the system (29).

$$\begin{cases} \dot{x} &= v_x, \\ \dot{y} &= v_y, \\ \dot{s} &= v_s, \\ \dot{v}_x &= g\frac{q}{m}\Big(v_s x\Big), \\ \dot{v}_y &= -g\frac{q}{m}\Big(v_s y\Big), \\ \dot{v}_s &= g\frac{q}{m}\Big(-v_x x + v_y y\Big). \end{cases} \tag{29}$$

2.6 Dimensionless system of equations for the quadrupole magnetic field in the curvilinear frame

Following the same approach as in the Section 2.4, we can change the variables by using the equations (30 - 32).

$$t = \tau \cdot \lambda. \tag{30}$$

$$\begin{cases} x &= c\tau \cdot \xi(\lambda), \\ y &= c\tau \cdot \zeta(\lambda), \\ s &= c\tau \cdot \eta(\lambda), \\ v_x &= c \cdot \varkappa_\xi(\lambda), \\ v_y &= c \cdot \varkappa_\zeta(\lambda), \\ v_s &= c \cdot \varkappa_\eta(\lambda). \end{cases} \tag{31}$$

$$\begin{cases} \dot{x} & = c \cdot \xi'(\lambda), \\ \dot{y} & = c \cdot \zeta'(\lambda), \\ \dot{s} & = c \cdot \eta'(\lambda), \\ \dot{v}_x & = \dfrac{c}{\tau} \cdot \varkappa_\xi{}'(\lambda), \\ \dot{v}_y & = \dfrac{c}{\tau} \cdot \varkappa_\zeta{}'(\lambda), \\ \dot{v}_s & = \dfrac{c}{\tau} \cdot \varkappa_\eta{}'(\lambda). \end{cases} \tag{32}$$

The dimensionless system of differential equations for the quadrupole field is expressed in the system (33).

$$\begin{cases} \xi'(\lambda) & = \varkappa_\xi(\lambda), \\ \zeta'(\lambda) & = \varkappa_\zeta(\lambda), \\ \eta'(\lambda) & = \varkappa_\eta(\lambda), \\ \varkappa_\xi{}'(\lambda) & = \left(g\dfrac{q}{m}\right) \cdot \left(c\tau^2\right) \cdot \varkappa_\eta(\lambda) \cdot \xi(\lambda), \\ \varkappa_\zeta{}'(\lambda) & = -\left(g\dfrac{q}{m}\right) \cdot \left(c\tau^2\right) \cdot \varkappa_\eta(\lambda) \cdot \zeta(\lambda), \\ \varkappa_\eta{}'(\lambda) & = \left(g\dfrac{q}{m}\right) \cdot \left(c\tau^2\right) \cdot \left(- \varkappa_\xi(\lambda) \cdot \xi(\lambda) + \varkappa_\zeta(\lambda) \cdot \zeta(\lambda)\right). \end{cases} \tag{33}$$

3 Considered elements of the ThomX ring

3.1 Electrodes

One of the methods to clear the ions is to place electrodes with constant electric field that is directed along x- or y-axes. In ThomX, we have 10 electrodes with the length of 0.1 m. Their central positions correspond to the maximums of the electric field in the Fig. 6, where the electric field along both $x-$ and y-axes is depicted.

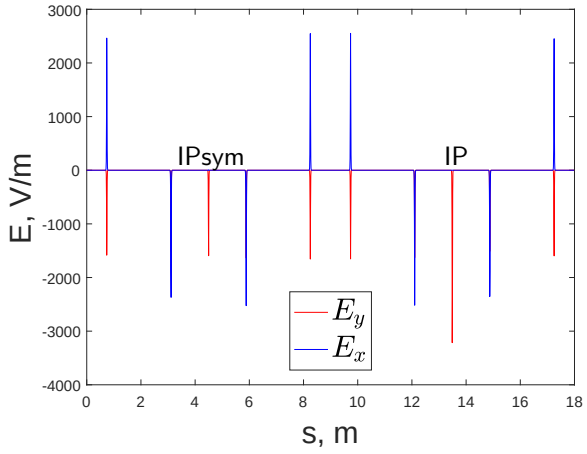

Figure 6: Electric field vs. longitudinal coordinate for one of the ThomX configurations. Signatures: Positions of the IP and IPsym points.

The CO^+ ion deviation only by electric field in one of the electrodes (without beam-ion interaction and magnetic fields) is depicted in the Fig. 7. Value $x = 0.15$ m corresponds to the edge of the pipeline. This ion was pushed into the wall and cleared.

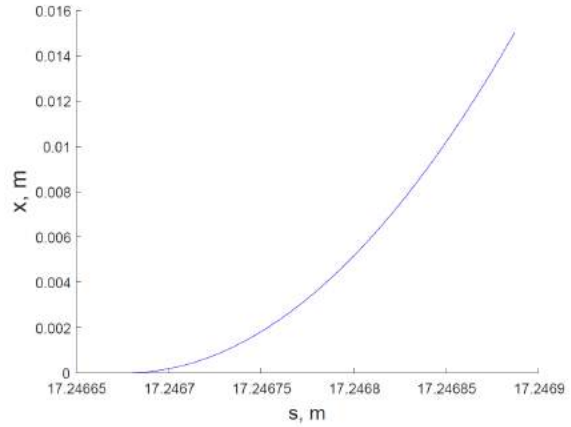

Figure 7: CO^+ ion deviation by electric field in the electrode (without beam-ion interaction and magnetic fields). Initial velocity of ion is tangent to the beam centerline.

Should notice, since the electron bunch has energy 50 MeV, the electric field from the electrodes does not perturb its trajectory and characteristics. However, it highly influences the movement of relatively slow ions by pushing them out of the beam space charge potential well.

Since our routine works for particles of different mass and charge, we tracked an electron as a test particle using all considered kicks: beam-ion interaction, electrodes, dipole and quadrupole magnets. As it was expected, the electron trajectory was straight (see Fig. 8).

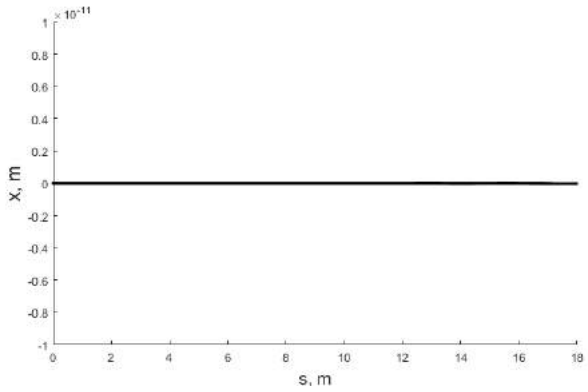

Figure 8: Electron trajectory in the ring.

3.2 Dipoles

The dipole magnetic field in ThomX (up to 0.6 T) is strong enough to make the orbit of the ions closed. That is why we expected to see the trapping in the dipole zones.

ThomX has 8 dipole magnets with bending radius of 0.352 m. The dipole magnetic field along the ThomX ring is depicted in the Fig. 9 (in the curvilinear frame, $x = 0$, $y = 0$).

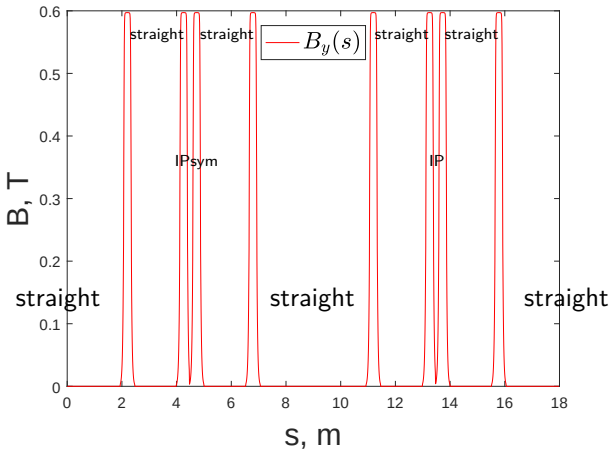

Figure 9: Dipole magnetic field vs. longitudinal coordinate.
Signatures: Placement of the straight sections, and IP and IPsym points.

If we consider only dipole magnetic field, the trajectory of a CO^+ ion with initial velocity v_s along the s-axis and initial position at the center of the dipole magnetic field is closed in the XS-plane (see Fig. 10).

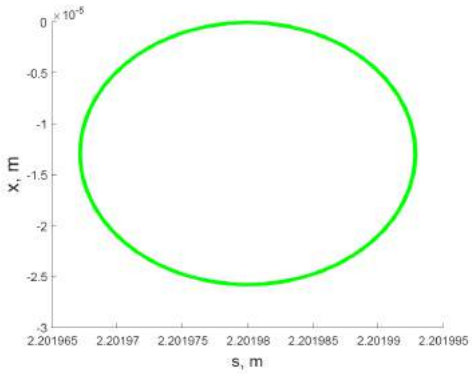

Figure 10: Closed orbit of CO^+ ion in the dipole (without beam-ion interaction, electrodes, and quadrupole field).

However, the ions that move along the s-axis towards the dipole magnet can be reflected by the fringe field (see Fig. 11, where only dipole field was considered). It is so called **mirror effect** [7].

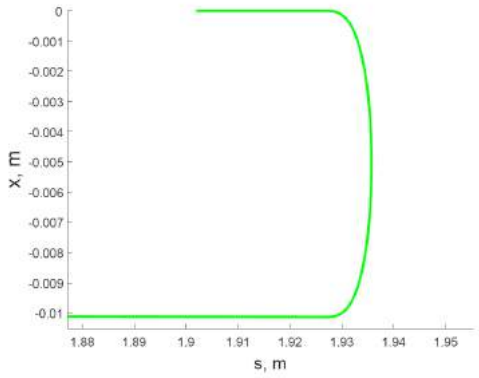

Figure 11: Reflection of CO^+ ion by dipole fringe field (without beam-ion interaction, electrodes, and quadrupole field).

3.3 Quadrupoles

Even though previous research [8] did not show the trapping in the quadrupoles (a value of the magnetic field is relatively small and does not influence ions on the beam centerline), we decided to check whether the combination of the beam-ion interaction and quadrupole magnetic field is really negligible.

The ThomX ring has 24 quadrupole magnets of 6 types with different values of the focusing strength ($k_1 = -4.53\ m^{-2}$; $k_2 = 9.26\ m^{-2}$; $k_3 = -17.74\ m^{-2}$; $k_4 = 15.19\ m^{-2}$; $k_5 = -12.06\ m^{-2}$; $k_6 = 8.62\ m^{-2}$). Their length is 0.15 m. Fig. 12 reflects the center positions of the quadrupoles.

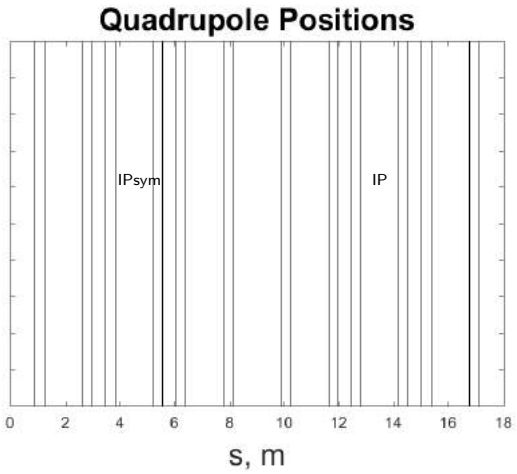

Figure 12: Quadrupole positions along the ThomX ring.

The trajectory of an ion with initial transverse coordinates $x = y = 0$ and velocity directed along the s-axis in the quadrupole magnet (without beam-ion interaction) is straight (see Fig. 13).

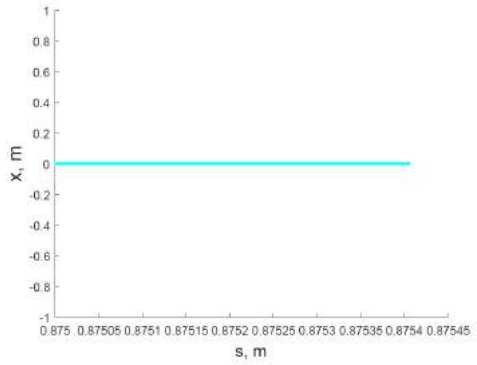

Figure 13: CO^+ ion trajectory with initial $x = y = 0$ and $v_x = v_y = 0$ in the quadrupole magnet (without beam-ion interaction).

The case for an ion out of the beam centerline ($x \neq 0$) is depicted in the Fig. 14.

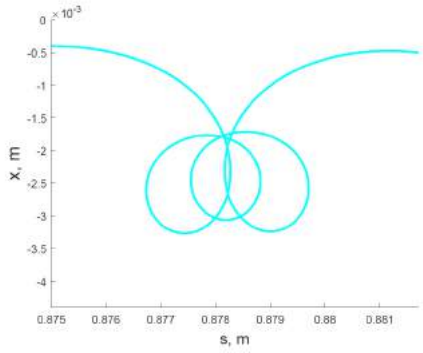

Figure 14: CO^+ ion trajectory with initial $x \neq 0$ and $v_x = v_y = 0$ in the quadrupole magnet (without beam-ion interaction).

3.4 Kickmap

Longitudinal kick expressed by formula (2) for CO^+ and $H_2{}^+$ ions is depicted in the Fig. 15. We see that the absolute value for the velocity increase of the $H_2{}^+$ ions is 14 times higher than the corresponding value for CO^+ ions. This is due to the higher mass of the latter. Around the IP and IPsym points, the longitudinal kick is directed towards the IP and IPsym points correspondingly. We also see the accumulation points marked as $*$. They are very close to the outer fringefields of the dipole magnets that are connected to the big straight sections of the ring. We expect to see the trapping at such accumulation points.

The parts to the right and to the left of the section in between two signs $*$ have very small longitudinal kicks. These parts correspond to the long (4127.5 mm) straight sections of the ThomX ring.

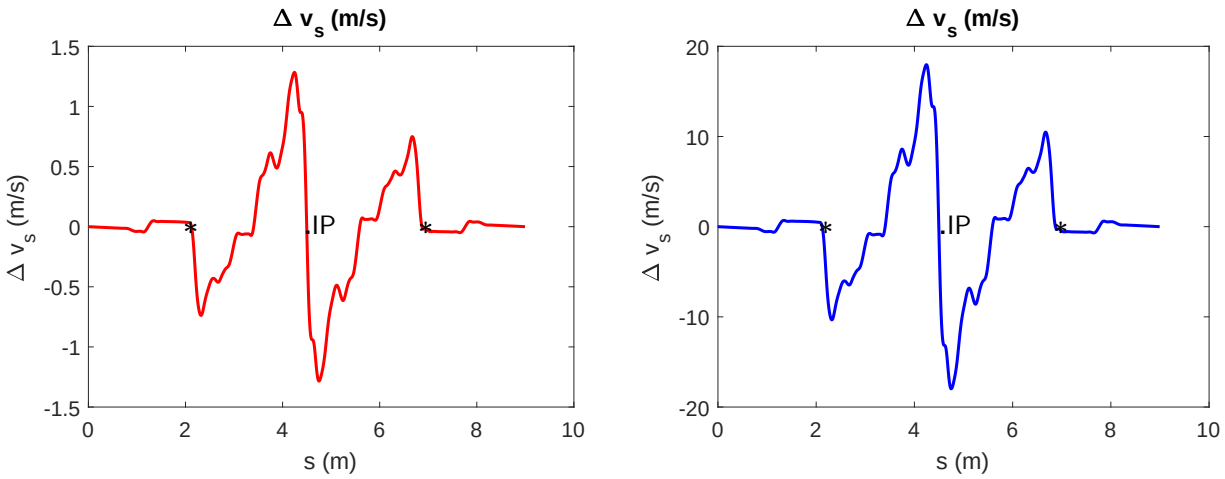

(a) CO^+ (b) $H_2{}^+$

Figure 15: Longitudinal kick Δv_s from the beam-ion interaction for ions with $x = 0$ and $y = 0$. The half of the ring.

Fig. 16 represents the transverse kick Δv_x from the formula 1 at the IP and IPsym points. It shows that ions placed close to the beam centerline have kicks towards the beam centerline. Should notice, the maximum absolute value on the x-axis of these two plots is equal to the maximum σ_x of the electron bunch in the ThomX ring. At the IP and IPsym points, the absolute value of σ_x is the smallest.

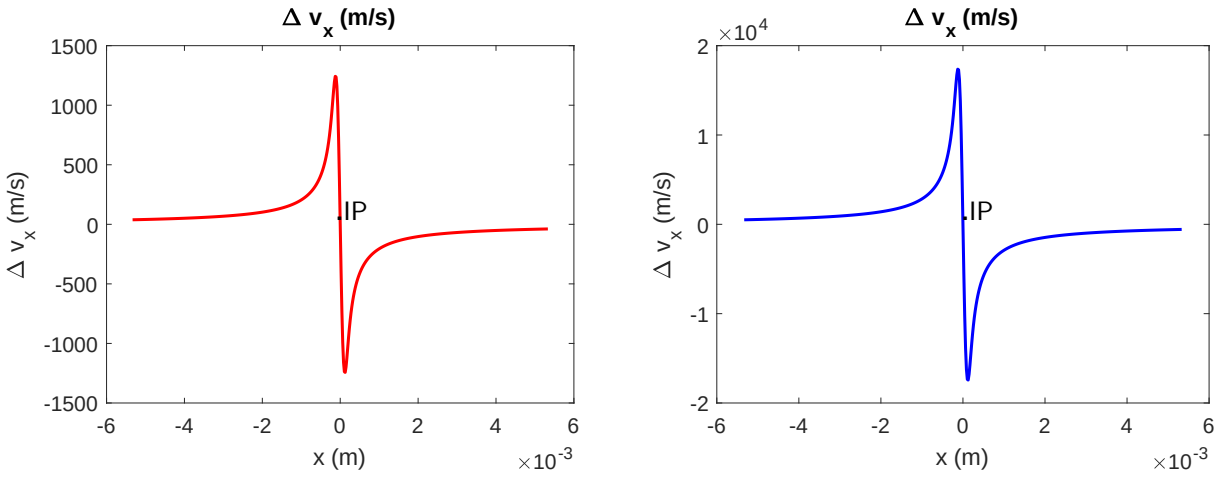

(a) CO^+ (b) $H_2{}^+$

Figure 16: Transverse kick Δv_x from the beam-ion interaction for ions with $y = 0$ at the IP and IPsym points ($s = 4.5$ m and $s = 13.5$ m respectively).

Fig. 17 and 18 show velocity increase for ions with velocities that correspond to the mean speed of the Boltzmann distribution at room temperature and are tangent to the reference trajectory. IP or IPsym points are placed directly at the center of each map. All elements (beam-ion interaction, electrodes, dipole and quadrupole magnets) are included.

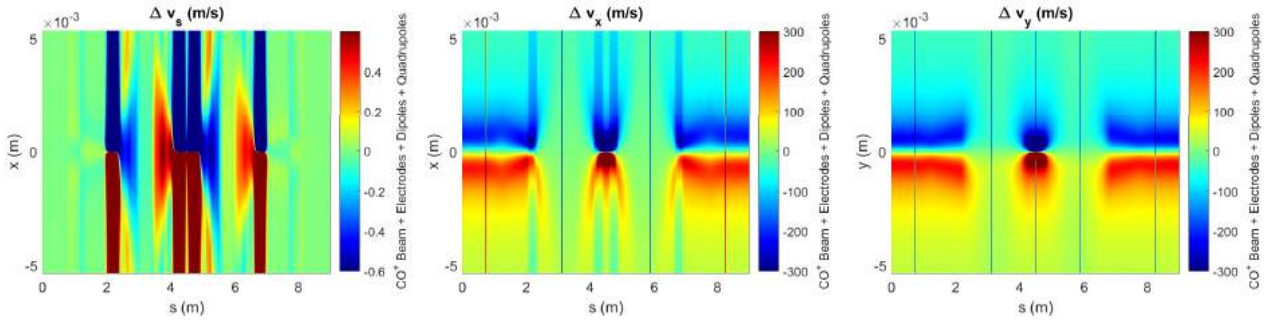

(a) Δv_s (b) Δv_x (c) Δv_y

Figure 17: Kickmap for CO^+. The half of the ring.

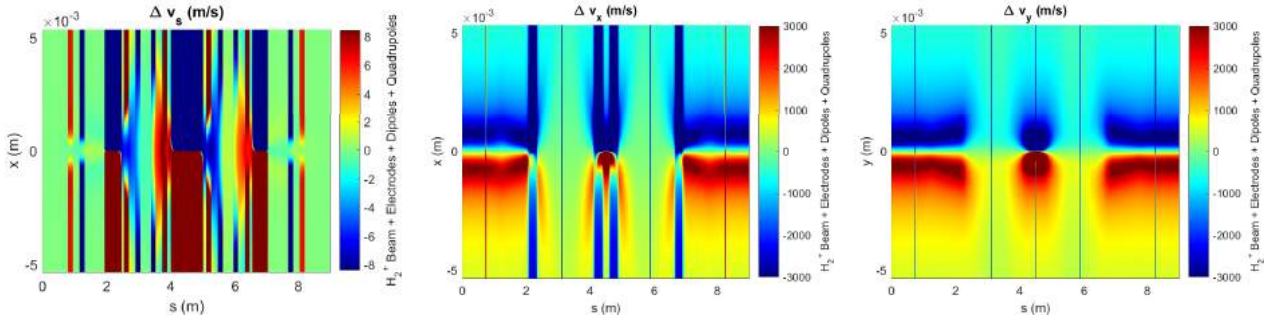

(a) Δv_s (b) Δv_x (c) Δv_y

Figure 18: Kickmap for $H_2{}^+$. The half of the ring.

In Fig. 17a for the longitudinal kick Δv_s of CO^+ ($y = 0$), we see that considered ions feel mainly the kicks from the beam-ion interaction (triangle-like shapes) and dipole magnets (solid vertical lines). The corresponding Fig. 18a for $H_2{}^+$ ions also shows the influence of the quadrupole magnets (narrow vertical lines) since the mass of $H_2{}^+$ ions is 14 times less. However, quadrupole kick is not visible directly near the beam centerline (the whole s-axis with $x = 0$).

In Fig. 17b and 18b for the transverse kick Δv_x ($y = 0$), the narrow vertical lines correspond to the E_x electrode field. If we compare these figures with Fig. 3 for only beam-ion interaction, we will see how the dipole magnetic field modifies the kickmap.

In Fig. 17c and 18c for the transverse kick Δv_y ($x = 0$), the narrow vertical lines correspond to the E_y electrode field. The other parts of the map belong to the beam-ion interaction. The dipole magnetic field does not give a kick in the direction of the y-axis and velocity increase from the quadrupole magnets is almost negligible.

4 Estimation of the number of ions in the ring

4.1 Ions created during the one turn

We consider that molecules CO and H_2 are distributed uniformly along the ring. The pressure in the pipeline is $p_0 \approx 3.06 \cdot 10^{-8}$ Pa [1]. The partial pressure of CO is $p_{CO} \approx 0.1 \cdot p_0$. For the H_2 molecules it is $p_{H_2} \approx 0.9 \cdot p_0$.

In order to find out how many new ions are created per one turn, we must know the ionization cross-section for the investigated molecules when an electron bunch is circulating in the ring. Required cross-sections were evaluated by using the formula (34) [9].

$$\sigma^i = 4\pi\left(\frac{\hbar}{m_e c}\right)^2\left\{M^2\left[\frac{1}{{\beta_e}^2}ln\left(\frac{{\beta_e}^2}{1-{\beta_e}^2}\right)-1\right]+\frac{C}{{\beta_e}^2}\right\} \tag{34}$$

$\hbar$ is the reduced Planck constant, m_e is the electron mass, β_e is equal to the ratio of electron velocity v_e and speed of light c. M^2 and C are constants that can be taken from the Tab. 1. Should notice, the ionization cross-section depends on the molecule of the residual gas and on the velocity of the ionizing particle but neither on its charge or its mass. The Formula (34) is empiric and, in general, coefficients M^2 and C are different for different molecules.

Molecule	M^2	C	Z	A
H_2	0.5	8.1	2	2
CO	3.7	35.1	14	28

Table 1: Value of the M^2 and C constants for calculation of ionization cross-section.

Concentration of molecules of sort i in the pipeline should be expressed by formula (35).

$$n_i = \frac{p_i}{k_B T} \tag{35}$$

Where p_i is the partial pressure, k_B is the Boltzmann constant, $T = (273.15 + 20)$ K is the room temperature in Kelvin.

Then the number of created ions per turn can be expressed from the values of the cross-section σ_i, number of electrons in the bunch $N_e = \frac{1\ \mathrm{nC}}{|e|}$, ring length L, and concentration n_i (36).

$$N^i_{new} = \sigma_i \cdot N_e \cdot L \cdot n_i. \tag{36}$$

For CO^+ ions $N^{CO^+}_{new} \approx 10$, and for ${H_2}^+$ ions $N^{{H_2}^+}_{new} \approx 17$.

4.2 Clearing coefficient of ion clearing

We consider a clearing coefficient of ion clearing as a function $\varepsilon(n)$ of the number of turns n passed by the electron bunch in the ring. It is defined as the number of ions in the ring $N_{ions}(n)$ at the turn n divided by the number of ions at the start of the simulation $N_0 = N_{ions}(0)$ (see Eq. 37).

$$\varepsilon(n) = \frac{N_{ions}(n)}{N_0}. \tag{37}$$

Further, we will consider the sequence of cycles with $4 \cdot 10^5$ turns of an electron bunch in the ring and small gaps of $4\ \mu s$ while the bunch is being replaced by new one and electron beam is absent in the ring. Also we will show the influence of the big gap when one full cycle is omitted and bunch does not circulate in the ring during 24 ms. The scheme of the sequence is depicted in the Fig. 19.

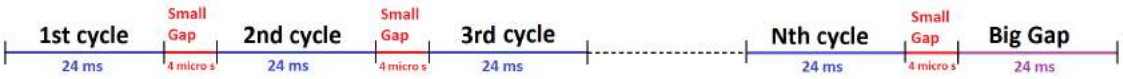

Figure 19: Scheme of the sequence of cycles and small gaps.

4.3 First cycle ($4 \cdot 10^5$ turns, or 24 ms)

The term **cycle** is used to denote the $4 \cdot 10^5$ turns while one bunch is moving in the ring. After each cycle, when the characteristics of the bunch degrade, this bunch must be replaced by new one with an extraction-injection system.

In order to estimate the number of ions for the first cycle ($4 \cdot 10^5$ turns) at each turn, we had to find an analytical way for calculation due to the large amount of created ions and, consequently, long time of simulation.

For this aim, we generated ions CO^+ and ${H_2}^+$ that were uniformly distributed along the ring in the logitudinal dimension and had Gaussian distribution with a standard deviation ($\pm\sigma_x$ and $\pm\sigma_y$) from the electron bunch parameters in the transverse plane [10]. From our simulation, we took the number of ions at each turn and divided it by the initial number of ions (in this case, $N_0 = 25\ 000$ for both types of ions). Obtained clearing coefficients are depicted in the Fig. 20.

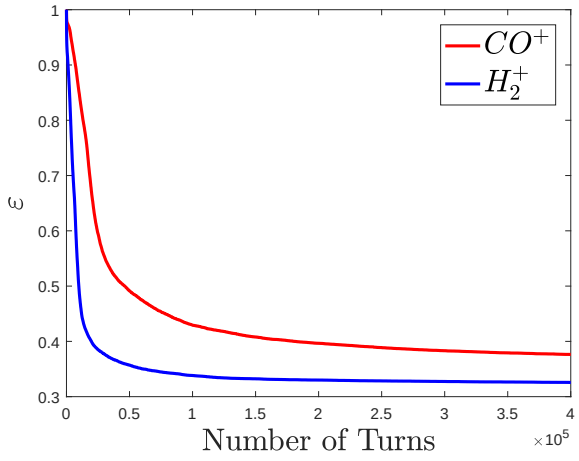

Figure 20: Clearing coefficient for the ions CO^+ and ${H_2}^+$ that were initially uniformly distributed along the ring.

At the beginning, we have $\varepsilon_{CO^+} = \varepsilon_{{H_2}^+} = 1$. Assumably, we have $N_{new}^{CO^+}$ and $N_{new}^{{H_2}^+}$ ions from the formula (36) that are uniformly distributed along the ring. The same number of ions as in the Eq. (38).

$$N_{ions}(0) = N_{new} \cdot \varepsilon(0). \tag{38}$$

After the first turn, this number is reduced to $N_{new} \cdot \varepsilon(1)$ (function $\varepsilon(n)$ is decreasing). However, we must consider also $N_{new} = N_{new} \cdot \varepsilon(0)$ new ions that were created during the first turn. It gives us Eq. (39).

$$N_{ions}(1) = N_{new} \cdot \varepsilon(0) + N_{new} \cdot \varepsilon(1). \tag{39}$$

After the second turn, we keep ions from the 0^{th} and 1^{st} turns and add $N_{new} \cdot \varepsilon(0)$ ions created during the second turn (40).

$$N_{ions}(2) = N_{new} \cdot \varepsilon(0) + N_{new} \cdot \varepsilon(1) + N_{new} \cdot \varepsilon(2). \tag{40}$$

Eq. (41) summarizes mentioned above.

$$\begin{aligned} N_{ions}(0) &= N_{new} \cdot \varepsilon(0), \\ N_{ions}(1) &= N_{new} \cdot \varepsilon(0) + N_{new} \cdot \varepsilon(1), \\ N_{ions}(2) &= N_{new} \cdot \varepsilon(0) + N_{new} \cdot \varepsilon(1) + N_{new} \cdot \varepsilon(2), \\ &\dots \\ N_{ions}(n) &= N_{new} \cdot \varepsilon(0) + N_{new} \cdot \varepsilon(1) + N_{new} \cdot \varepsilon(2) + \dots + N_{new} \cdot \varepsilon(n). \end{aligned} \tag{41}$$

Eq. (41) can be rewritten as the integral (42).

$$N_{ions}(n) = N_{new} \cdot \int_0^n \varepsilon(z) dz. \tag{42}$$

Thus the number of ions for each step of the first cycle can be obtained by integration of the curve from the Fig. 20. This dependency is depicted in the Fig. 21.

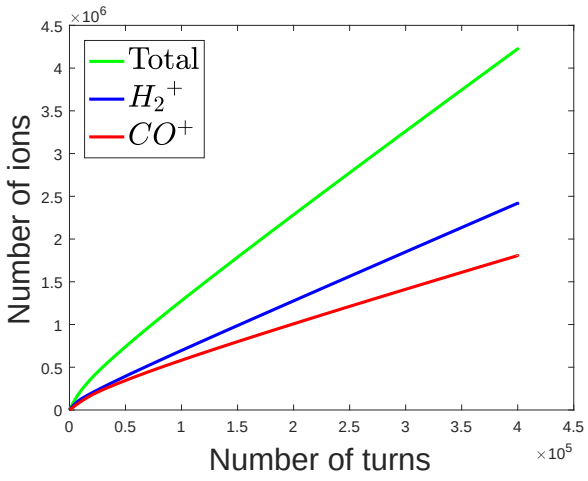

Figure 21: Number of ions CO^+ and $H_2{}^+$ that were initially uniformly distributed along the ring.

Investigation of the evolution of the longitudinal ion positions helps us to understand whether the ring has zones where the concentration of the ions is the highest.

At the start of simulation, we generated the ions that had uniform longitudinal distribution and Gaussian distribution with a standard deviation ($\pm\sigma_x$ and $\pm\sigma_y$) of the electron bunch in the transverse plane. Then tracked them for $4 \cdot 10^5$ turns.

In Fig. 22 and 23, the horizontal axis corresponds to the longitudinal positions of the ions. The color on the colorbar represents the number of ions at these longitudinal positions.

The number on the vertical scale multiplied by 50 gives the number of a turn at which we check the longitudinal distribution.

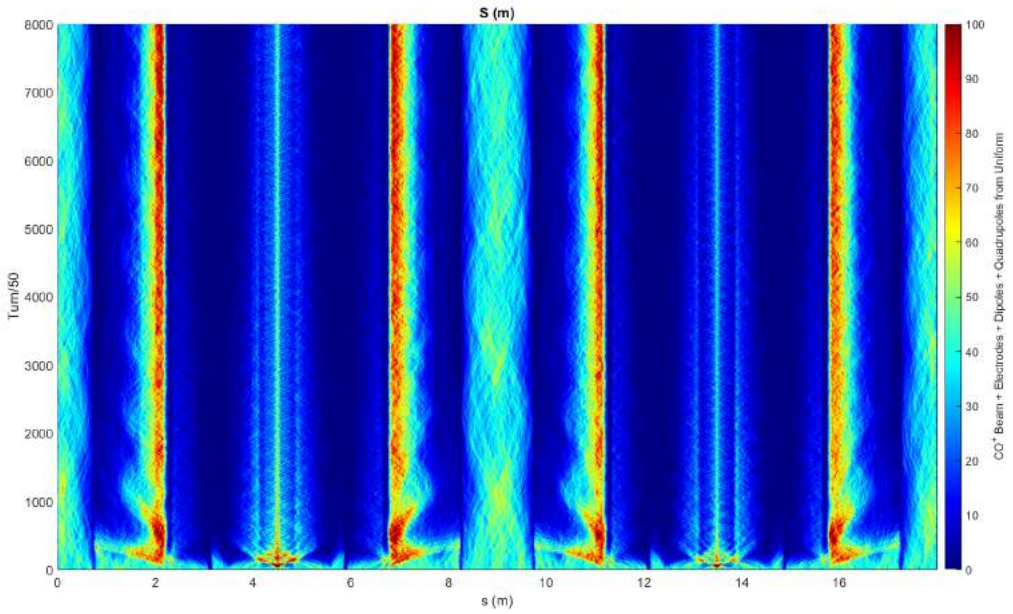

Figure 22: Longitudinal distribution of CO^+ ions. Initial distribution is uniform.

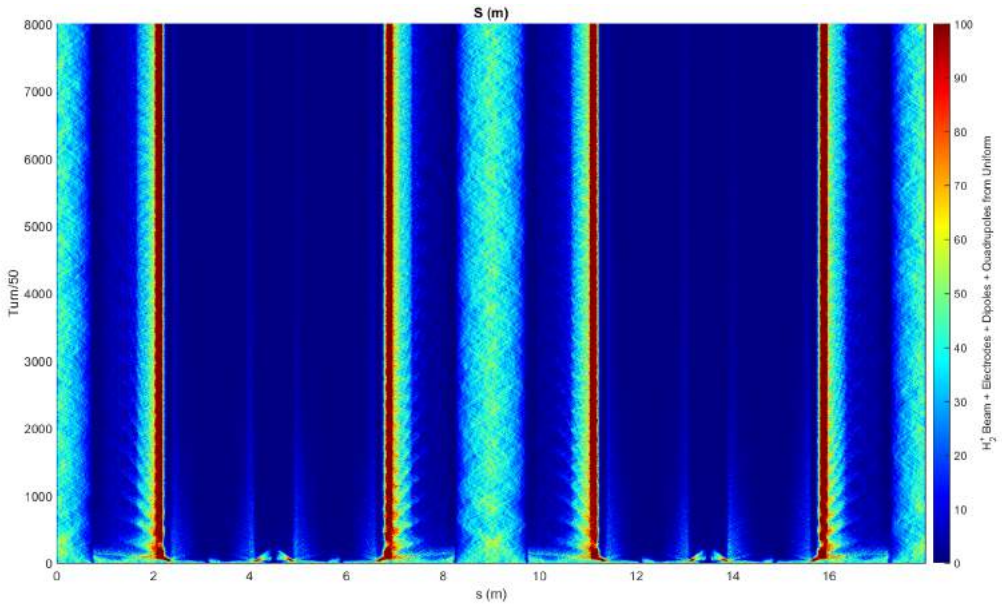

Figure 23: Longitudinal distribution of $H_2{}^+$ ions. Initial distribution is uniform.

Analysis of the Fig. 22 and 23 gives following conclusions:

- Blue-green wide vertical zones correspond to two long straight sections of the ring ((16-18 m; 0-2 m) and 7-11 m). The longitudinal kicks on these sections are relatively small (see Fig. 15). It means that ions created on the long straight sections stay on those sections.

- Red vertical lines correspond to the points in the Fig. 15 marked as $*$. These are accumulation points because the longitudinal kicks are directed towards them. The origin of the vertical lines at the IP and IPsym for CO^+ ions is the same. However, since we have the clearing electrodes at the IP and IPsym, we do not see these lines for the $H_2{}^+$ ions.
- Increasing the electric field of the electrodes at the IP and IPsym, we can reduce the number of CO^+ ions at these points. However, it will not change the total number of ions in the ring dramatically, because the ratio of the number of ions at IP and IPsym to the total number is negligibly small.
- The CO^+ ions are slower than the $H_2{}^+$ ions. That is why they move to stable zones slower.
- Stable zones are stable roughly after $4 \cdot 10^4$ turns (10% of the full cycle).

Comparison of the Fig. 24 for the distribution of CO^+ and $H_2{}^+$ ions at the final turn of the simulation with the shape of the dipole magnetic field B_y, electric field of electrodes $E_{x,y}$, and optical function β_x in the Fig. 25 leads to the conclusion that most of the ions are trapped around and inside the dipoles and straight sections.

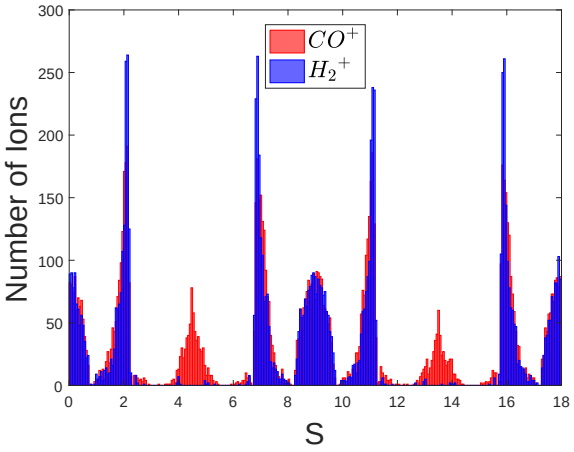

Figure 24: Longitudinal distribution of CO^+ and $H_2{}^+$ ions at the final turn of the first cycle.

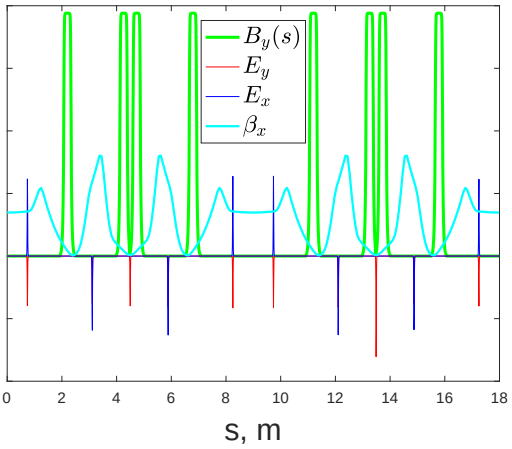

Figure 25: Longitudinal dependence of the dipole field, electric field and β_x optical function.

On the Fig. 24, the number of survived ions is 9 413 out of 25 000 for CO^+ and 8 146 out of 25 000 for $H_2{}^+$. 43% of the survived ions of both types are trapped inside the dipole magnets. The other ions are mostly concentrated around the dipoles (near the fringe field – see Section 5.1) and on the straight parts of the ring.

4.4 Small gap (66 turns, or 4 μs)

Small gap is a short (up to $4\mu s$) period between the cycles without an electron bunch in the ring. Thus no beam-ion interaction, but trapping in the dipole magnetic field is possible.

Roughly 50% of the ions after the first $4 \cdot 10^5$ turns were out of the dipole magnetic field zones. Sufficiently large gap could allow them to escape from the beam centerline. For ions in the dipole magnetic field, the only possibility was to escape thanks to the kick along the y-axis. The latter kick is not changed by dipole field.

We took the final distribution of ions after the simulation for the first $4 \cdot 10^5$ turns as the initial for the tracking without beam-ion interaction. Thus we found out that small gap does not reduce the number of CO^+ ions in the ring (see clearing coefficient in the Fig. 27), but rather changes their transverse distribution (Fig. 26a for CO^+ and Fig. 26b for $H_2{}^+$) by giving them a chance to escape the trapping in the beam space charge potential.

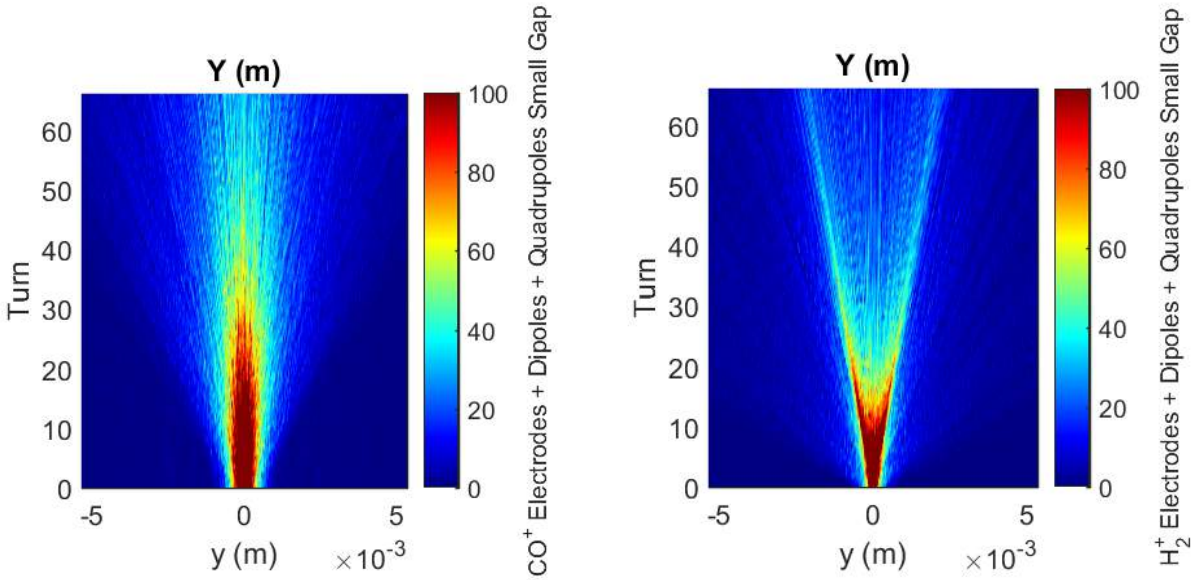

(a) CO^+ (b) $H_2{}^+$

Figure 26: Transverse distribution of all ions in the ring during the small gap.

Since the CO^+ ions are slower than $H_2{}^+$, they escape slower. It means that we clear them worse. Comparison of the clearing efficiency of ion clearing for the CO^+ and $H_2{}^+$ ions is depicted in the Fig. 27.

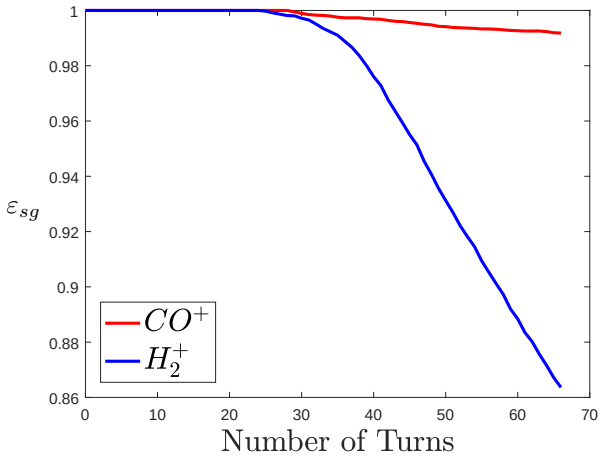

Figure 27: Clearing coefficient for the ions CO^+ and $H_2{}^+$ during the small gap (66 turns) after the tracking through the first cycle.

Should notice, the initial number of CO^+ ions at the beginning of the small gap in this case was bigger than the initial number of $H_2{}^+$, because the $H_2{}^+$ ions were better cleared after the first $4 \cdot 10^5$ turns of simulation.

In order to evaluate the effect of the small gap on a large amount of cycles, we developed an analytical approach. If we denote the clearing coefficient function $\varepsilon(n)$ from the Fig. 27 as $\varepsilon_{sg}(n)$, then the number of ions during the small gap can be estimated with the known number of ions after the first cycle ($N_{\text{first cycle}} = N_{new} \cdot \int_0^{n_{cycle}} \varepsilon(z)dz$) as in the Eq. (43), where $n_{cycle} = 4 \cdot 10^5$ turns and $n_{sg} = 66$ turns.

$$N_{ions}(n) = \underbrace{\underbrace{N_{new} \cdot \left(\int_0^{n_{cycle}} \varepsilon(z)dz \right)}_{\text{After the first cycle}} \cdot \varepsilon_{sg}(n) =}_{\text{During the first small gap}} \tag{43}$$
$$= N_a \cdot \varepsilon_{sg}(n), \; n \in [0, \; n_{sg}].$$

N_a from the Eq. (43) denotes the number of ions that are still alive at the end of the previous part of tracking (in this case, at the end of the first cycle).

The number of ions for the first cycle with the first small gap is depicted in the Fig. 28.

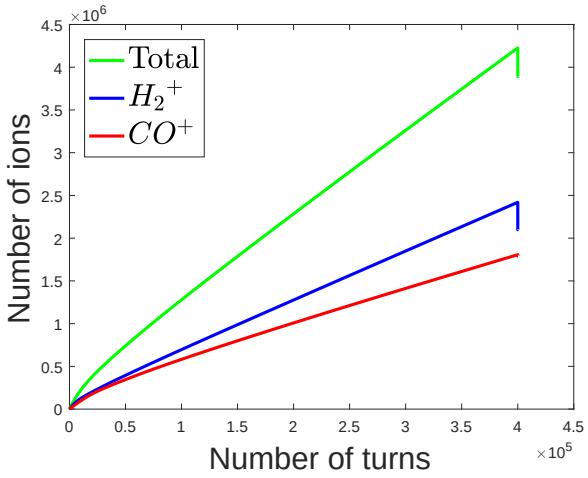

Figure 28: Number of ions CO^+ and $H_2{}^+$ during the first cycle and small gap (from Eq. (42 – 43)).

4.5 Second cycle and second small gap

Since most of the ions after $4 \cdot 10^5$ turns are distributed non-uniformly along the ring (see Fig. 24), some places have higher concentration of the ions. We call them stable regions, stable zones, or stable states. At the same time, redistribution of the ions in the transverse plane after the small gap changes ion characteristics as well. Furthermore, the number of CO^+ after the tracking via the first cycle and small gap is higher than the number of $H_2{}^+$. Thus an expected behaviour of the clearing coefficient function $\varepsilon(n)$ must be different from the case for the first cycle (was shown in the Fig. 20).

Tracking the ions through the first $4 \cdot 10^5$ turns, small gap, and the next cycle of $4 \cdot 10^5$ turns, we obtained the function $\varepsilon_a(n)$ for the second cycle for those ions that survived after the first cycle (Fig. 29).

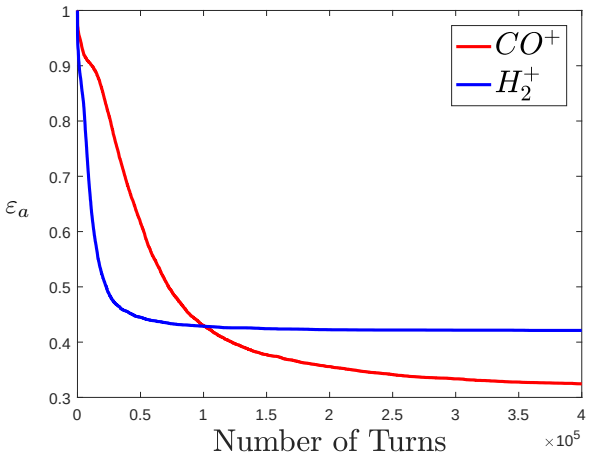

Figure 29: Clearing efficiencies for the ions CO^+ and $H_2{}^+$ that were non-uniformly distributed along the ring.

$H_2{}^+$ ions after the small gap reach their accumulation points faster. At these points, we cannot clear them properly while the electron is present in the ring. It explains the higher clearing coefficient for the $H_2{}^+$ at the end of the second cycle of simulation.

Fig. 30 and 31 prove that surviving ions continue their movement within the stable zones afterwards. Moreover, we see that after the small gap all the CO^+ ions at the IP and IPsym points were eventually cleared by the electrodes.

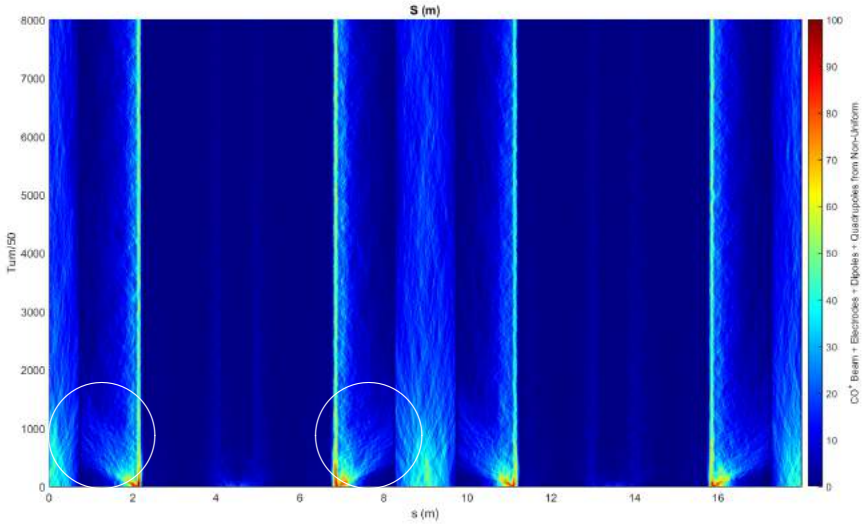

Figure 30: Longitudinal distribution of CO^+ ions. Initial distribution is non-uniform.

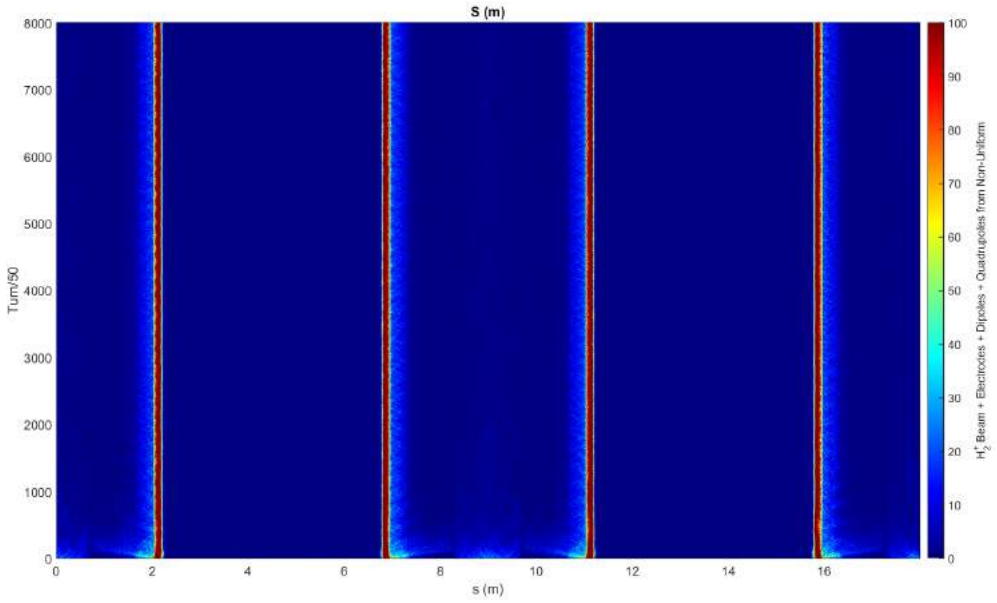

Figure 31: Longitudinal distribution of $H_2{}^+$ ions. Initial distribution is non-uniform.

In Fig. 30 in white circles, we clearly see the clearing of the CO^+ ions by the electrodes placed at $s = 0.74$ m and $s = 8.25$ m. Ions move towards accumulation points, but are intercepted by the electric field.

In order to generalize the evolution of the number of ions in the ring for many cycles, let us consider the number of all the ions that were not neutralized after the first cycle and first small gap (are alive) as N_a, their number during the second cycle will reduce as a function (44), where $\varepsilon_a(n)$ is a clearing coefficient function $\varepsilon(n)$ for the second cycle from the Fig. 29.

$$N(n) = N_a \cdot \varepsilon_a(n),\ n \in [0,\ n_{cycle}]. \tag{44}$$

At the same time, besides the mentioned alive ions, N_{new} new ions will be created each turn. Taking the equations (42) and (44) together, we get the equation (45) for the number of ions during the second cycle of $4 \cdot 10^5$ turns. This equation can be used for all the next cycles of $4 \cdot 10^5$ turns. The number N_a must be taken as the number of alive ions at the end of the preceding small gap.

$$N_{ions}(n) = N_a \cdot \varepsilon_a(n) + N_{new} \cdot \int_0^n \varepsilon(z)dz,\ n \in [0,\ n_{cycle}]. \tag{45}$$

Taking into account Eq. (43), we can rewrite the value N_a after the first small gap with the following equation (46), where $n_{sg} = 66$ turns for the small gap.

$$N_a = \underbrace{\underbrace{N_{new} \cdot \left(\int_0^{n_{cycle}} \varepsilon(z)dz \right)}_{\text{After the first cycle}} \cdot \varepsilon_{sg}(n_{sg})}_{\text{After the first small gap}}. \tag{46}$$

Thus we get Eq. (47) for the number of ions during the second cycle.

$$N_{ions}(n) = \underbrace{\underbrace{N_{new} \cdot \left(\int_0^{n_{cycle}} \varepsilon(z)dz \right) \cdot \varepsilon_{sg}(n_{sg})}_{\text{After the first small gap}} \cdot \varepsilon_a(n) + N_{new} \cdot \int_0^{n} \varepsilon(z)dz}_{\text{During the second cycle}}, \; n \in [0, \; n_{cycle}]. \tag{47}$$

Formula for the number of ions during the second small gap can be obtained by fixing the number of alive ions N_a after the second cycle and multiplying this number by clearing coefficient for the small gap $\varepsilon_{sg}(n)$ (48).

$$N_{ions}(n) = \underbrace{\underbrace{\left[N_{new} \cdot \left(\int_0^{n_{cycle}} \varepsilon(z)dz \right) \cdot \varepsilon_{sg}(n_{sg}) \cdot \varepsilon_a(n_{cycle}) + N_{new} \cdot \left(\int_0^{n_{cycle}} \varepsilon(z)dz \right) \right]}_{\text{After the second cycle}} \cdot \varepsilon_{sg}(n)}_{\text{During the second small gap}},$$
$$n \in [0, \; n_{sg}]. \tag{48}$$

Two cycles with two small gaps are depicted in the Fig. 32.

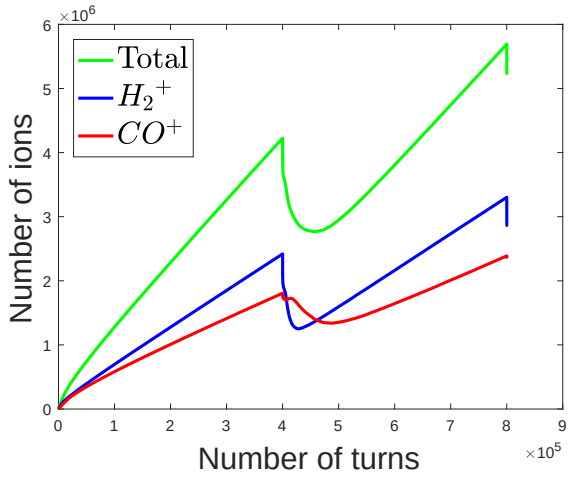

Figure 32: Number of ions CO^+ and $H_2{}^+$ during the first two cycles with small gaps (from Eq. (42 – 48)).

After the second small gap we have different value of N_a (49), which must be taken as the initial number of ions in the ring for the third cycle.

$$N_a = \underbrace{\underbrace{\left[N_{new} \cdot \left(\int_0^{n_{cycle}} \varepsilon(z)dz \right) \cdot \varepsilon_{sg}(n_{sg}) \cdot \varepsilon_a(n) + N_{new} \cdot \left(\int_0^{n_{cycle}} \varepsilon(z)dz \right) \right]}_{\text{After the second cycle}} \cdot \varepsilon_{sg}(n_{sg})}_{\text{After the second small gap}}. \tag{49}$$

4.6 Big gap ($4 \cdot 10^5$ turns without an electron bunch)

Big gap is a cycle without an electron bunch. We did not inject new bunch and thus omit the whole cycle just to clear all the ions.

The clearing coefficient function $\varepsilon_{bg}(n)$ for the big gap is depicted in the Fig. 33. It proves that after $1.5 \cdot 10^5$ turns we dramatically reduce the number of ions in the ring. However, some ions can survive.

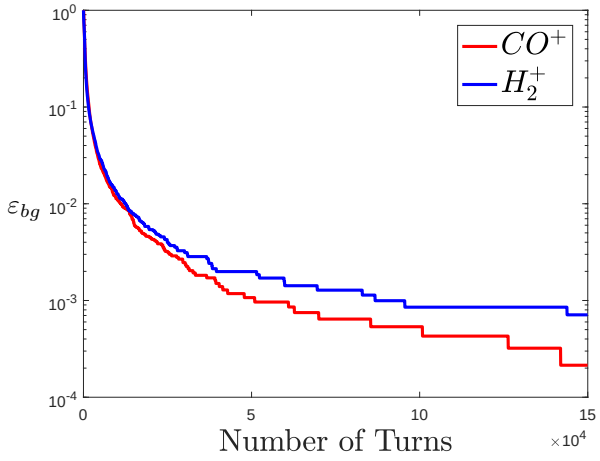

Figure 33: Clearing coefficient for the ions CO^+ and $H_2{}^+$ during the $1.5 \cdot 10^5$ turns without an electron bunch.

Should notice, the initial number of CO^+ ions at the beginning of the big gap in this case is not the same as the initial number of $H_2{}^+$. The initial distribution of ions for the big gap was taken after the tracking through the second small gap.

Following our analytical approach, we denote the number of ions in the ring before the big gap was N_a, the number of ions during the big gap can be computed with the following formula (50), where $n_{bg} = n_{cycle} = 4 \cdot 10^5$ turns.

$$N_{ions}(n) = N_a \cdot \varepsilon_{bg}(n), \ n \in [0, \ n_{bg}]. \tag{50}$$

4.7 Summarizing formula

Summarizing description above, we can write equation for the number of ions within one cycle, small gap, and big gap as in the Eq. (51), where N_a always denotes the number of ions that were not neutralized after the previous part of tracking.

$$\begin{cases} \text{Cycle: } N_{ions}(n) = N_a \cdot \varepsilon_a(n) + N_{new} \cdot \int_0^n \varepsilon(z)dz, \ n \in [0, \ n_{cycle}], \\ \text{Small gap: } N_{ions}(n) = N_a \cdot \varepsilon_{sg}(n), \ n \in [0, \ n_{sg}], \\ \text{Big gap: } N_{ions}(n) = N_a \cdot \varepsilon_{bg}(n), \ n \in [0, \ n_{bg} = n_{cycle}]. \end{cases} \tag{51}$$

Fig. 34 shows the variation of the number of ions during the first 10 cycles with small gaps and big gap at the end.

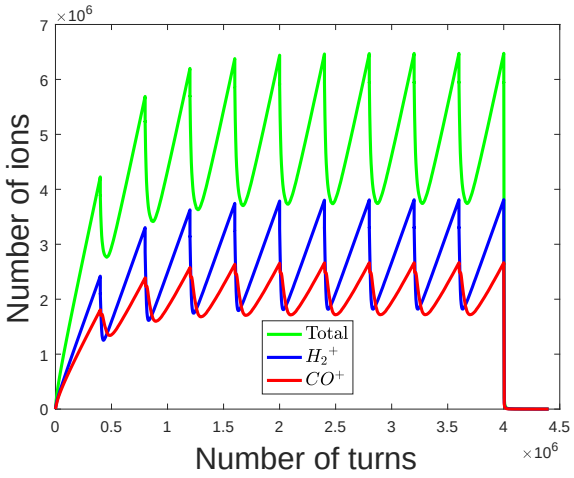

Figure 34: Number of ions CO^+ and $H_2{}^+$ during the first 10 cycles with small gaps and final big gap with $4 \cdot 10^5$ turns without an electron bunch.

The neutralization factor (number of ions related to the number of electrons) in the ring is negligible. Thus the singly-ionized ions are not a problem for the ThomX ring thanks to clearing with electrodes abd small gaps.

5 Discussion

5.1 Stable zones

Analysis of the Fig. 35 for the distribution of ions after the whole cycle while their initial distribution was uniform, and Fig. 36 where this distribution is plotted with the behaviour of the dipole magnetic field B_y, electrode field $E_{x,y}$, and optical function β_x shows that residual ions are mostly concentrated near the dipole fringe fields and on the straight sections. The accumulation of the ions on the straight sections between the dipole magnets can be explained by combination of so called **mirror effect** (see Fig. 11) and small longitudinal kicks from beam-ion interaction. This effect assumes that the longitudinal gradient of the magnetic field may reverse the ion motion thus creating a barrier; for this reason sections between magnets must incorporate clearing electrodes [7]. ThomX has such electrodes on the straight parts of the ring (spaces between non-zero sections of the dipole magnetic field B_y in the Fig. 36): at 17246.68, 740, 8250.24, 9736.44, and 3110.21 5883.13, 12103.55, 14876.47 mm.

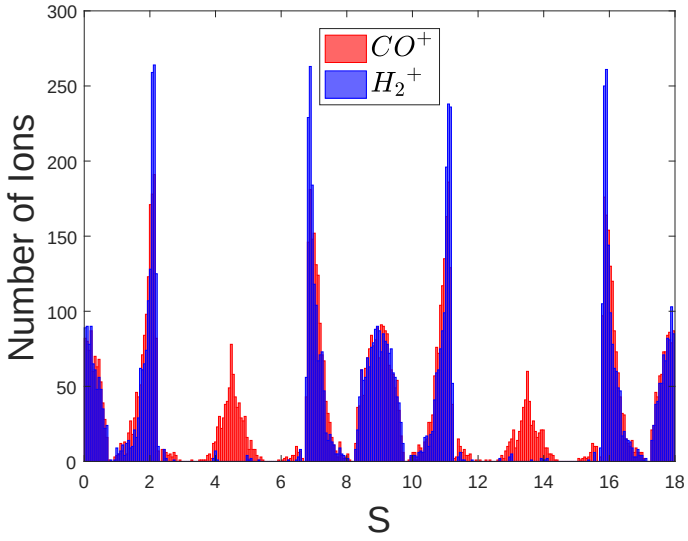

Figure 35: Longitudinal distribution of CO^+ and $H_2{}^+$ ions after the $4 \cdot 10^5$ turns from uniform distribution.

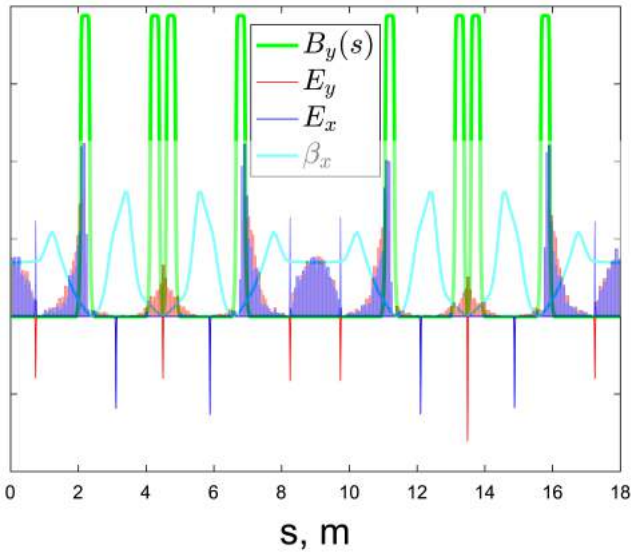

Figure 36: Fig. 35 with the behaviour of B_y, $E_{x,y}$, β_x.

5.2 Without electrodes

Since, increasing the electric field in all the electrodes by factors 1.5 and 2, we did not find better clearing, it was important to understand the contribution of the electrodes to ion clearing in the ThomX ring. Results show that without electrodes we almost do not clean the CO^+ ions (Fig. 37b).

Judging from the Fig. 37 for the comparison of the final distributions with and without electrodes, electrodes that correspond to the negative electric field E_x are positioned directly near the places of the lowest expectable accumulation of ions. Yet they help to clear the CO^+ ions from that move due to the longitudinal kicks from the beam-ion interaction to the accumulation points (see Fig. 15).

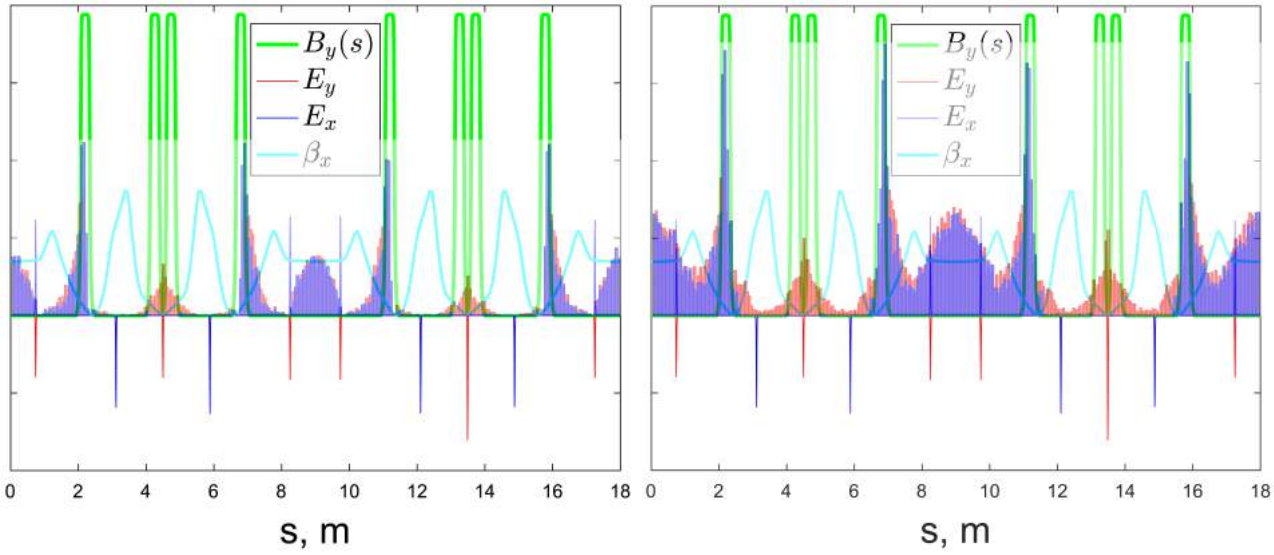

(a) **With** electrodes. (b) **Without** electrodes.

Figure 37: Comparison of the final distribution of ions that were initially uniformly distributed along the ring after the whole cycle with the behaviour of B_y, $E_{x,y}$, β_x with and without electrodes.

Fig. 38 represents the difference in the clearing coefficients for the case with and without electrodes. As it was expected, electrodes help to reduce the number of ions in the ring. However, trying to increase the electrode field for the all electrodes in the ring 1.5 or 2 times, we did not get a decrease of the clearing coefficient.

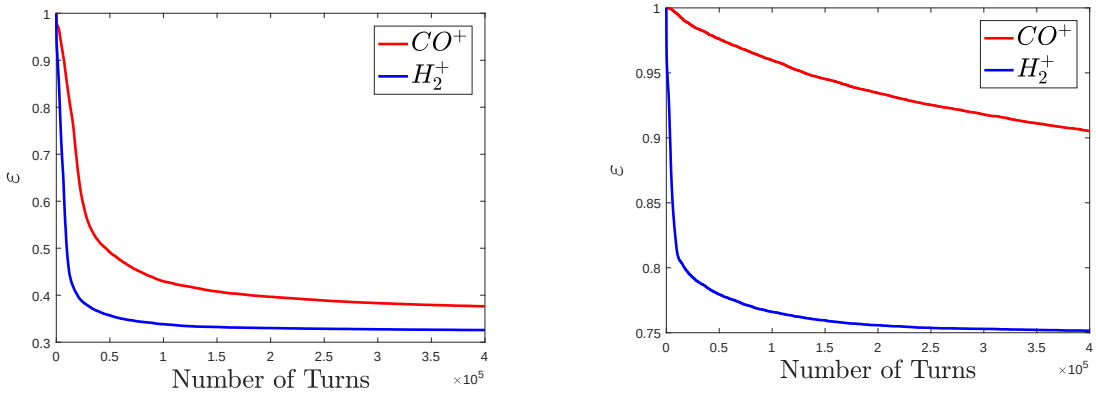

(a) **With** electrodes. (b) **Without** electrodes.

Figure 38: Comparison of the clearing coefficient for the ions CO^+ and $H_2{}^+$ that were initially uniformly distributed along the ring with and without electrodes.

Comparison of the number of ions in the ring is depicted in the Fig. 39. The case without electrodes gives roughly 5 times higher number.

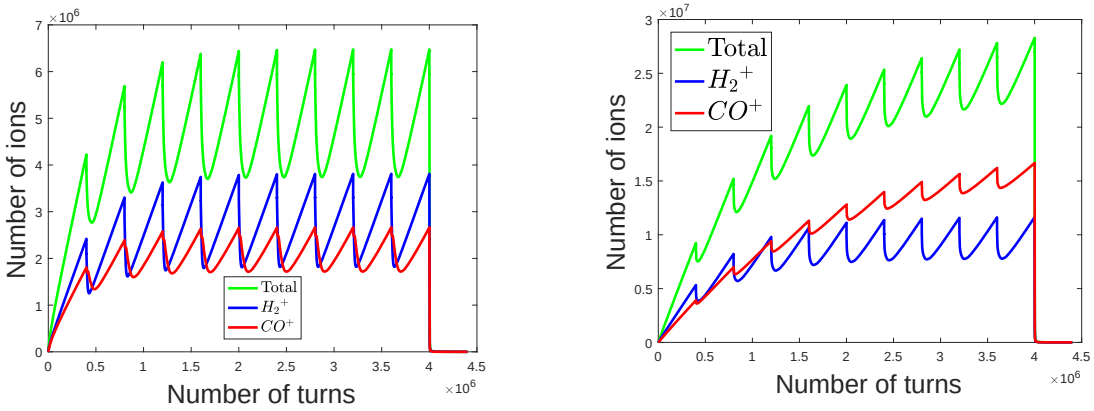

(a) **With** electrodes.

(b) **Without** electrodes.

Figure 39: Comparison of the number of ions CO^+ and $H_2{}^+$ during the first 10 cycles with small gaps and big gap at the end with and without electrodes.

5.3 Without small gaps

In order to reduce working hours of the ThomX accelerator, it is reasonable to make small gaps for the extraction-injection as small as possible (less than $4\mu s$). However, our computation proved that without small gaps we would have dramatic increase of the number of ions in the ring.

Fig. 40a demonstrates what would happen without the small gaps (but with electrodes) after 10 cycles. It shows that without small gaps total number of ions is increasing and limited only by the total number of residual gas molecules (Fig. 40b).

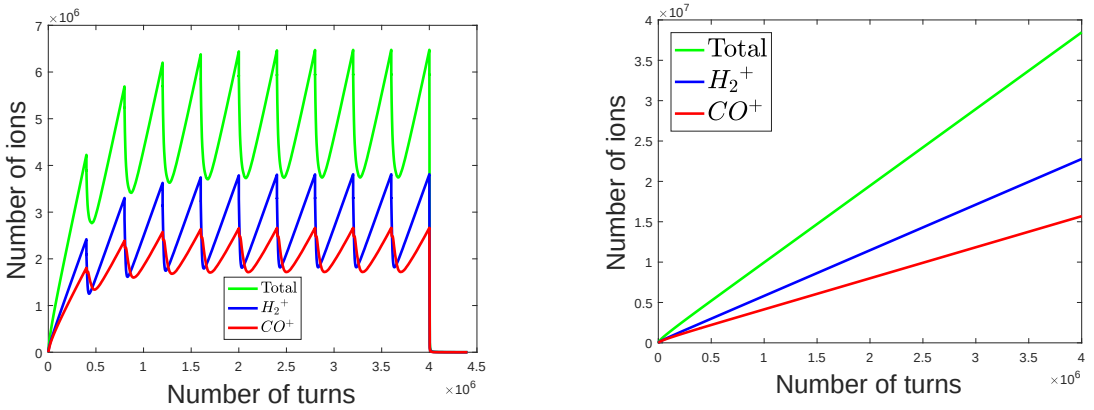

(a) **With** small gaps.

(b) **Without** small gaps.

Figure 40: Comparison of the number of ions CO^+ and $H_2{}^+$ during the first 10 cycles with and without small gaps (with electrodes).

6 Conclusions

- Interaction of the residual gas with beam was considered. However, only for single ionization.

- Ion tracking with the beam-ion interaction, ion movement in dipole and quadrupole magnetic fields was implemented.
- We cannot say that trapping at the points of the highest accumulation is due to the dipole magnets only. It is rather a combination of the mirror effect from dipole fringe field and beam-ion interaction that makes ions move to the dipoles.
- Quadrupole influence is almost negligible for the residual ions.
- 1.5 or 2 times increase of the electrode field did not change our results.
- Small gaps are important for the ion clearing. The longer gap, the better.
- Multi-ionization of the residual gas requires additional research.

References

[1] A. Variola, J. Haissinski, A. Loulergue, F. Zomer, eds, "ThomX Technical Design Report." 2014.

[2] D. Sagan, "Some a spects of the longitudinal motion of ions in electron storage ring", Nucl. Instrum. Methods, A307 p.171 (1991).

[3] A. Poncet, "Ion trapping and clearing," in *"Frontiers of Particle Beams: Factories with e^+e^- Rings"*, edited by M. Dienes, M. Month, B. Strasser, and S. Turner, Lecture Notes in Physics, Vol. 425, pp. 202–221, Springer, Berlin Heidelberg, 1994.

[4] A. Gamelin, C. Bruni, "Residual Ion Dynamics in ThomX Electron Storage Ring", in *Proc. 7th International Particle Accelerator Conference (IPAC'16)*, Busan, Korea, Mar. 2016, paper TUPOR002, pp. 1648–1650, ISBN: 978-3-95450-147-2, 2016.

[5] A. Tkatchenko, "DEA Physique et technologie des grands instruments. Mouvement d'une particule chargée dans un champ magnétique (courbure et focalisation transverse)."

[6] A. Latina, "Introduction to Transverse Beam Dynamics. Lecture 1: Magnetic fields and particle trajectories," JUAS 2014, January 13th, 2014.

[7] Poncet A. (1992) "Ions and neutralization." In: Dienes M., Month M., Turner S. (eds) "Frontiers of Particle Beams: Intensity Limitations. Lecture Notes in Physics, vol. 400." Springer, Berlin, Heidelberg.

[8] K. Ohmi and S. Matsumoto, "Beam-ion instability in a magnetic field," Conf. Proc. C **9803233**, 438 (1998).

[9] Y. Baconnier, A. Poncet, and P.F. Tavares, "Neutralisation of accelerator beams by ionisation of the residual gas," Jyvaeskylae (Finland) 1992, CERN 94-10.

[10] T.O. Raubenheimer and F. Zimmermann, "A Fast Beam-Ion Instability in Linear Accelerators and Storage Rings," SLAC-PUB-95-6740.